11-21-2018

Graphene Used as a Lateral Force Microscopy Calibration Material in the Low-Load Non-Linear Regime

Mathias J. Boland
University of Kentucky, mbo233@uky.edu

Jacob L. Hempel
University of Kentucky, jacob.hempel@uky.edu

Armin Ansary
University of Kentucky, armin.ansary@uky.edu

Mohsen Nasseri
University of Kentucky, mohsen.nasseri@gmail.com

Douglas R. Strachan
University of Kentucky, doug.strachan@uky.edu

Graphene Used as a Lateral Force Microscopy Calibration Material in the Low-Load Non-Linear Regime

Notes/Citation Information
Published in *Review of Scientific Instruments*, v. 89, issue 11, 113902, p. 1-9.

This article appeared in *Review of Scientific Instruments*, v. 89, issue 11, 113902, p. 1-9 and may be found at https://doi.org/10.1063/1.5044727.

Digital Object Identifier (DOI)
https://doi.org/10.1063/1.5044727

Review of Scientific Instruments

Graphene used as a lateral force microscopy calibration material in the low-load non-linear regime

Cite as: Rev. Sci. Instrum. **89**, 113902 (2018); https://doi.org/10.1063/1.5044727
Submitted: 15 June 2018 . Accepted: 01 November 2018 . Published Online: 21 November 2018

Mathias J. Boland, Jacob L. Hempel, Armin Ansary, Mohsen Nasseri, and Douglas R. Strachan

Graphene used as a lateral force microscopy calibration material in the low-load non-linear regime

Mathias J. Boland,[a] Jacob L. Hempel,[a] Armin Ansary, Mohsen Nasseri, and Douglas R. Strachan[b]
Department of Physics and Astronomy, University of Kentucky, Lexington, Kentucky 40506, USA

(Received 15 June 2018; accepted 1 November 2018; published online 21 November 2018)

A lateral force microscopy (LFM) calibration technique utilizing a random low-profile surface is proposed that is successfully employed in the low-load non-linear frictional regime using a single layer of graphene on a supporting oxide substrate. This calibration at low loads and on low friction surfaces like graphene has the benefit of helping to limit the wear of the LFM tip during the calibration procedure. Moreover, the low-profiles of the calibration surface characteristic of these layered 2D materials, on standard polished oxide substrates, result in a nearly constant frictional, adhesive, and elastic response as the tip slides over the surface, making the determination of the calibration coefficient robust. Through a detailed calibration analysis that takes into account non-linear frictional response, it is found that the adhesion is best described by a nearly constant vertical orientation, rather than the more commonly encountered normally directed adhesion, as the single asperity passes over the low-profile graphene-coated oxide surface. *Published by AIP Publishing.* https://doi.org/10.1063/1.5044727

I. INTRODUCTION

Lateral force microscopy (LFM), also known as frictional force microscopy (FFM), is an enormously powerful scanning probe measurement technique that can provide insight into nanomechanical and nano-tribological properties.[1,2] In contrast to topographic imaging and vertical force measurement,[3–5] which is easily calibrated using a known z-piezo displacement and a thermal tune,[6–8] the relation between the measured lateral voltage signal and the actual lateral force is not easily discernable. In large part, this is due to the lateral displacement of the reflected laser spot being a relatively stiff torsional flexing, compared to the softer vertical flexural bending, of the cantilever. The vertical displacement for most AFM tips occurs over a size scale large enough to directly control and probe with the AFM, whereas the torsional flexing is accompanied by extremely small displacements of the tip that are typically beyond the scanning resolution of the entire AFM-sample configuration.[9] Moreover, since the frictional and contact forces of a very sharp single-asperity tip sliding over a surface can be altered significantly as the tip wears,[10] it is strongly beneficial to have a calibration method that preserves its structural integrity. Complicating this issue further is that the LFM calibration coefficient must be determined for each cantilever, making it extremely important to utilize a fast and inexpensive calibration method that does not damage the delicate tip.[11,12]

Over the last two decades, there have been a number of techniques used to ascertain LFM calibration coefficients.[11–34] Perhaps the most commonly used technique is the "wedge" method initially conceived of by Ogletree *et al.*[13] and later extended by Varenberg *et al.*[18] The wedge method utilizes the resulting LFM signals as the tip laterally slides over the surface of crystal gratings of known contrasting surface angles in order to calibrate the entire cantilever, optical lever arm, and photo-detector lateral system in a single-step calibration procedure.[13] A deficiency in this calibration method is that it is typically performed at large enough normal loads of the cantilever such that Amonton's law,[35] i.e., the proportionality of frictional force to normal load, is maintained. Unfortunately, these large normal loads applied during the calibration can result in wear and tear on the tip that can adversely affect subsequent LFM investigations of surfaces. Thus, it is advantageous to perform the calibration using as small a normal load as possible and to perform it on low-friction surfaces. However, it is well known that as the normal load for a single asperity is reduced to zero, the commonly used linear relation of Amonton's law is not necessarily valid—instead, often being better described by sub-linear frictional behavior.[36] This makes the common wedge calibration suspect in the low-load single-asperity regime, with recent work showing that it becomes unreliable once the load is reduced to values comparable to the adhesion.[30,34] Thus, a low-load LFM calibration method valid in a regime typically dominated by a non-linear frictional response can be of significant use for maintaining the integrity of small-diameter single-asperity scanning probe tips.

The necessity of a fast and reliable low-load lateral calibration method has increased in recent years as few-layer graphene and related 2D materials have risen in prominence and LFM has proven to be effective at probing their nanoscale properties.[37–52] Here we show that a single layer of graphene exfoliated on a supporting oxide substrate, the quintessential sample at the heart of these emergent 2D materials, can actually be used as just such a low-load LFM calibration surface valid in the low-load non-linear frictional regime. Essentially, the technique we describe here is the wedge method extended into the non-linear regime employing a low-friction low-profile random surface topography, one that is typical for an

[a]Mathias J. Boland and Jacob L. Hempel contributed equally to this work.
[b]Author to whom correspondence should be addressed: doug.strachan@uky.edu

atomically thin 2D material (such as graphene) situated on a typical substrate surface.

The use of an atomically thin 2D material, like graphene, as a LFM calibration surface has a number of important advantages. The method can be performed in the low-load (non-linear) regime that helps to preserve the single-asperity LFM tip during the calibration step. Moreover, 2D materials (like graphene) generally have low frictional forces that can help to preserve the integrity of the nanoscale tip during calibration. The low friction of 2D materials also allows for easier calibration since the correction terms (due to non-linear friction) are minimized. In addition, exfoliated 2D materials on typical oxide surfaces are materials that have recently become readily available and as such provide convenient surfaces to achieve low-friction low-profile surfaces useful for this calibration. And finally, the low-profiles of the calibration surface characteristic of these layered 2D materials result in a nearly constant frictional, adhesive, and elastic response as the tip slides over the surface, making the determination of the calibration coefficient more robust.

Overall, we show that graphene is a straightforward surface to use for reproducibly determining the cantilever calibration for LFM in the low-load non-linear frictional regime. In fact, through our detailed calibration analysis, we find that the non-linear frictional response has a much smaller effect on the calibration than the correct adhesion modeling. Our modeling suggests that the adhesion maintains a nearly vertical orientation as the single asperity passes over the low profile of a typical graphene-coated oxide surface.

Below, we first provide an overview and analytic derivation of the LFM calibration in the low-load non-linear regime over low-profile surfaces with small-angle topographic changes. In this first part, the non-linear calibration methodology is compared and contrasted to a linear calibration that assumes Amonton's law of frictional response. In the second part of this report, we perform this non-linear calibration analysis on LFM data on single-layer graphene. The results of the non-linear analysis show that the method yields a consistent determination of the LFM calibration coefficient down to extremely low net loads (defined as applied load plus adhesion) of about 2 nN.

II. LFM CALIBRATION IN THE LOW-PROFILE NON-LINEAR REGIME

In most LFM experimental configurations, a relation between a lateral force T on a tip and the measured voltage signal (typically obtained from photo-detectors) can be assumed of the form

$$V = V_0 + T/\alpha, \tag{1}$$

where V is the measured voltage, V_0 is the voltage baseline offset, T is the lateral force, and α is the calibration coefficient connecting the voltage to the lateral force.[13,18] The α calibration coefficient is non-trivial to determine and critical for obtaining quantitative lateral force determination.

To derive the LFM calibration coefficient in the non-linear regime for a random low-profile sample surface, we begin with the free-body diagram of an LFM cantilever in the lateral force mode as it slides over a local incline of small angle θ, as shown in Fig. 1. In this figure, we have also shown an atomically thin 2D material that conforms to the surface of a bulk substrate. Experiments[53] and theory[54] are well-known to support this picture of a thin 2D material conforming to the low-profile topographic features of a supporting substrate.

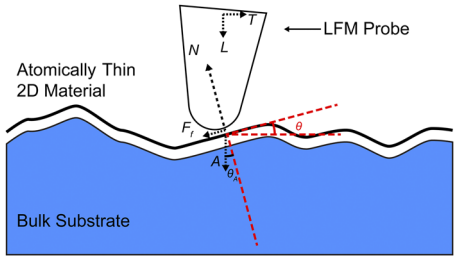

FIG. 1. Force diagram for the system. The adhesion angle, θ_A, is zero for the case of vertical adhesion, while it is equal to θ, the local angle of incline at the tip-surface contact, for normal adhesion.

Since the tip is not accelerating, the forces perpendicular and parallel to the incline add to 0, yielding

$$\sum F_{\parallel} = T_t \cos\theta - L\sin\theta - F_{f_t} - A\sin\theta_A = 0 \tag{2}$$

and

$$\sum F_{\perp} = -T_t \sin\theta - L\cos\theta + N - A\cos\theta_A = 0, \tag{3}$$

where the subscript of t denotes the trace forces (i.e., the forces in sliding from the left to the right in Fig. 1), L is the load applied to the tip by the AFM system, T_t is the trace force exerted on the tip to push it along the surface, and N is the normal force acting on the tip. There is also an adhesive force, A, which pulls the tip at an angle θ_A, with respect to the normal. We model the LFM tip system considering two cases, when the adhesion force is directed normal to the incline plane, giving $\theta_A = 0$, and when it is directed vertically, giving $\theta_A = \theta$, as shown in Fig. 1. To keep the discussion general, we will parameterize the adhesion with the small angle θ_A throughout the derivation.

The term F_{f_t} in Eq. (1) is the frictional force in the trace direction. In a linear regime, it is assumed that this frictional force obeys Amonton's law such that $F_{f_t} = \mu N$, with μ being the standard coefficient of kinetic friction. However, at low loads for single asperities, non-linear behavior is expected, as illustrated by the solid red curve in Fig. 2. While a general

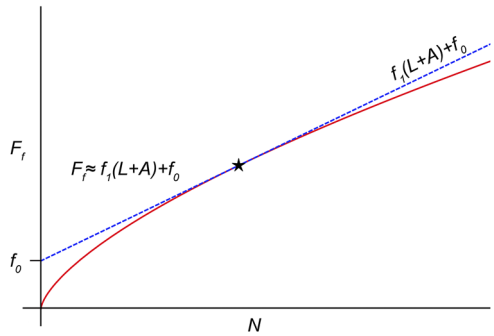

FIG. 2. Sketch of typical low-load non-linear frictional response (solid red curve) for a single asperity. The region about the starred point can be approximated by a linearized expansion (dashed blue curve), where the slope is given by f_1.

analytic formulation of the tip response utilizing the complete non-linear force is non-trivial, as long as the low-load response is analytic, we can approximate its behavior in a small regime by the linearized expansion of the form

$$F_{f_t} = f_0 + f_1 N. \tag{4}$$

In this expression, f_0 and f_1 are, respectively, the y-intercept (a force) and slope (with dimensions of a friction coefficient) of the approximation valid in the vicinity of the intersection with the nonlinear behavior, as shown by the dashed blue line in Fig. 2.

Utilizing the approximate force in Eq. (4), the normal force can be eliminated from Eqs. (2) and (3) and solved for T_t,

$$T_t = \frac{L(\sin\theta + f_1\cos\theta) + A(\sin\theta_A + f_1\cos\theta_A) + f_0}{\cos\theta - f_1\sin\theta}, \tag{5}$$

and applying the small angle approximation, we arrive at

$$T_t \approx \frac{L(\theta + f_1) + A(\theta_A + f_1) + f_0}{1 - f_1\theta}. \tag{6}$$

For the retrace results (denoted by a subscript r), we likewise find

$$T_r \approx \frac{L(\theta - f_1) + A(\theta_A - f_1) - f_0}{1 + f_1\theta}. \tag{7}$$

We will now relate the transvers forces (T_t and T_r) to the measured lateral voltage signals. The lateral voltage signals for a given load and position will have both a trace value (V_t) and retrace value (V_r). In order to determine the calibration coefficient, we relate it to the experimentally determined half-difference of these voltages,

$$W_V \equiv \frac{V_t - V_r}{2}, \tag{8}$$

and their zeroed average,

$$\Delta_{V_0} \equiv \frac{V_t + V_r}{2} - V_0. \tag{9}$$

Inserting Eqs. (1), (6), and (7) into Eqs. (8) and (9) yields, to linear order in the small angles θ and θ_A,

$$W_V = \frac{1}{2\alpha}(T_t - T_r) \approx \frac{f_1(L + A) + f_0}{\alpha}, \tag{10}$$

and

$$\Delta_{V_0} = \frac{1}{2\alpha}(T_t + T_r) \approx \frac{\theta\left[L\left(1 + f_1^2\right) + f_1^2 A + f_0 f_1\right] + A\theta_A}{\alpha}. \tag{11}$$

Provided there is an analytic relation between θ and θ_A, we can obtain the local value of θ as a function of the experimentally measured W_V and Δ_{V_0}. The first model we consider is an adhesion angle directed *normally* to the inclined surface, as is typical for macroscopic surfaces, such that $\theta_A = 0$ and yielding, according to Eq. (11),

$$\theta_{norm} = \frac{\alpha\Delta_{V_0}}{(L + A)f_1^2 + L + f_0 f_1}. \tag{12}$$

Over extremely small surface features (relevant to graphene on a polished oxide surface), an alternative model of the adhesion angle is one where it remains constant and directed *vertically* toward the average surface plane—a plane that averages over the small atomic-scale height variations of the surface. In this scenario, $\theta_A = \theta$, yielding, according to Eq. (11),

$$\theta_{vert} = \frac{\alpha\Delta_{V_0}}{(L + A)(f_1^2 + 1 + \frac{f_0 f_1}{L+A})}. \tag{13}$$

Equation (10) can be used to solve for f_1, yielding

$$f_1 = \frac{\alpha W_V - f_0}{L + A}, \tag{14}$$

which can be inserted into Eqs. (12) and (13) to solve for these surface angles as a function of the experimentally determined W_V and Δ_{V_0}. Equation (14) implies that $f_1 + \frac{f_0}{L+A} = \frac{\alpha W_V}{L+A}$ and $f_1 = \alpha\frac{dW_V}{d(L+A)}$, which can both be used in Eqs. (12) and (13) to obtain

$$\theta_{norm} = \frac{\alpha\Delta_{V_0}}{L + (L + A)\alpha^2\left(\frac{dW_V}{d(L+A)}\right)\left(\frac{W_V}{(L+A)}\right)}, \tag{15}$$

and

$$\theta_{vert} = \frac{\alpha\Delta_{V_0}}{(L + A)\left[1 + \alpha^2\left(\frac{dW_V}{d(L+A)}\right)\left(\frac{W_V}{(L+A)}\right)\right]}. \tag{16}$$

Equations (15) and (16) can be compared to the surface angles determined through low-profile topography

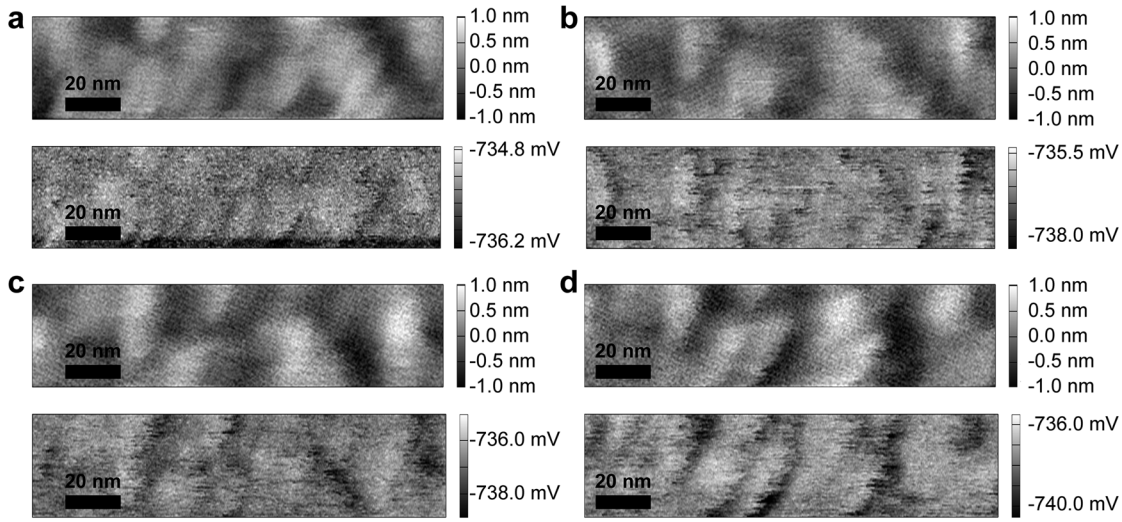

FIG. 3. Simultaneously obtained topography (upper panels) and LFM scans (lower panels) for four different loads. Net loads for (a), (b), (c), and (d) are 4, 10, 14, and 20 nN, respectively.

measurements made of the surface, given by $\theta_{topo}(x) = \frac{dH(x)}{dx}$, where $\theta_{topo}(x)$ is the surface angle, $H(x)$ is the topography, and x is in the fast scan direction. By matching the surface angles from the two measurements, the calibration coefficient α can be determined.

It is important to note that Eqs. (15) and (16) are valid in a regime of a nonlinear frictional response, with the derivative $\frac{dW_V}{d(L+A)}$ computed at the value of $(L + A)$. In a linear response regime, the derivative, $\frac{dW_V}{d(L+A)}$, simplifies to $\frac{W_V}{(L+A)}$, and Eqs. (15) and (16) become identical to results derived previously that assume Amonton's law for the friction.[42]

It is also important to note that as the applied load L increases, the adhesion becomes insignificant in the model and θ_{norm} and θ_{vert} converge to the same value. Thus, the correct identification of the adhesion angle θ_A is only significant at low-loads—i.e., the same regime typically characterized by a nonlinear frictional response.

III. LOW-LOAD LFM CALIBRATION USING GRAPHENE

To test our low-load non-linear LFM methodology, we have utilized well-known sticky-tape exfoliation of 2D layered materials[55–57] to place a single-layer of graphene

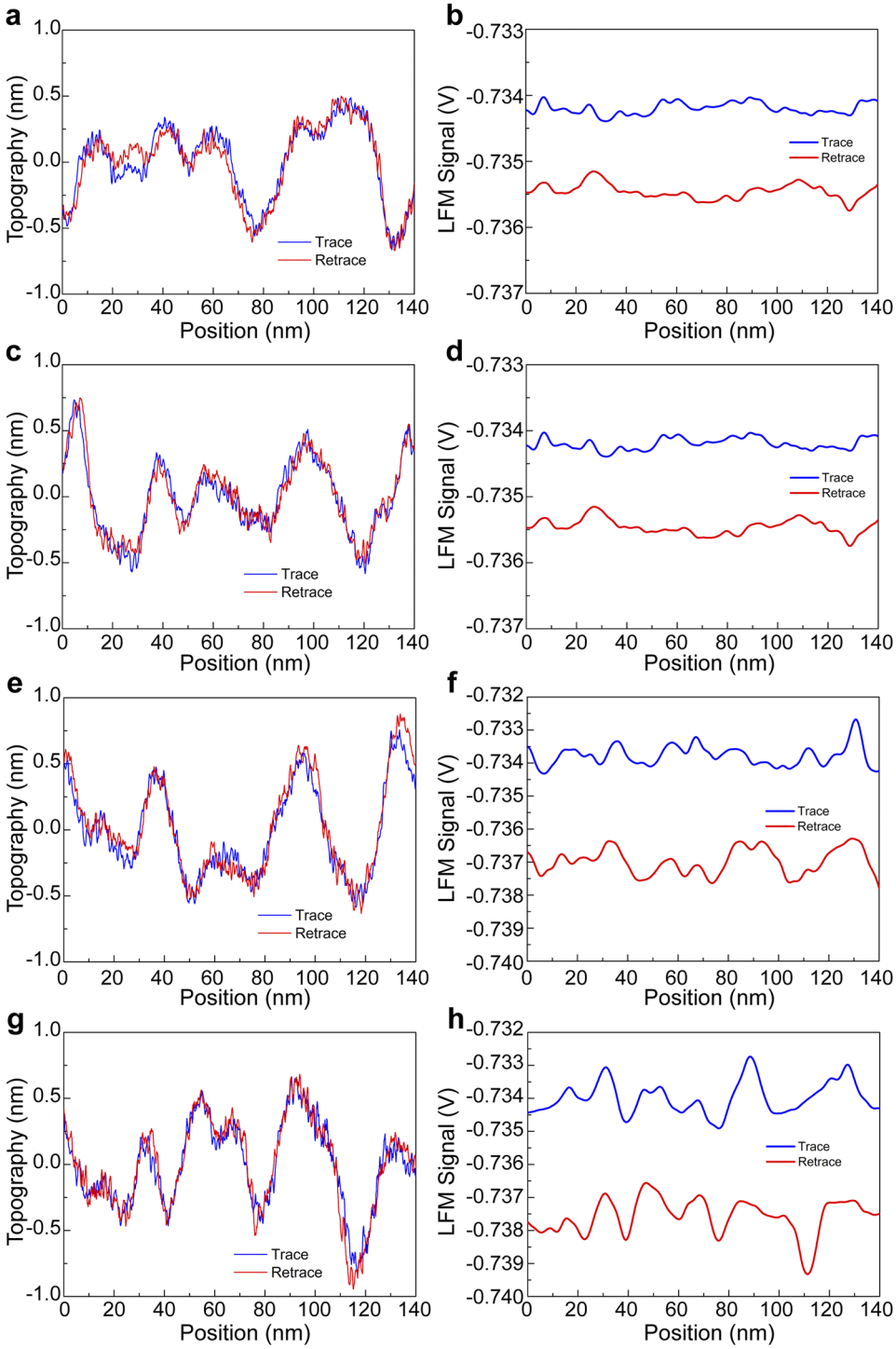

FIG. 4. Plots of trace and retrace measurements at characteristic loads for topography [(a), (c), (e), and (g)] and the corresponding LFM voltage signals [(b), (d), (f), and (h), respectively], with the trace signal being the upper line in each panel. Net loads are 4 nN [(a) and (b)], 10 nN [(c) and (d)], 14 nN [(e) and (f)], and 20 nN [(g) and (h)]. Signals are an average of 5 line scans over ~2.9 nm. A low pass filter has been applied to the LFM signals.

onto a polished (<1 nm RMS surface roughness) thermally grown SiO_2 substrate (300 nm thick oxide on a p-doped Si wafer). For this test, we have simultaneously acquired the topography and the raw lateral signals using an Asylum Research MFP-3D AFM using Nanosensors PPP-LFMR probes. All measurements were performed in ambient laboratory conditions (~20 °C). LFM scans were taken at a relatively slow scan speed of ~0.13 μm/s. At these low speeds, the friction between the probe and graphene should be approximately velocity independent.[58] Additionally, the low profile of the graphene substrate ensures that the scan speed over the surface is approximately constant during measurement, something that further reduces frictional velocity dependence.[38]

Figure 3 shows scanned topography and LFM images of a region of our graphene sample for various loads, while Fig. 4 shows corresponding line scans from these images for both trace and retrace directions. It is clear from the results in Fig. 4 that the topography is reproduced regardless of the scan direction, whereas the LFM signal has an offset between the scans that reflects the frictional response according to Eq. (10). Since Eq. (10) is valid in the small angle approximation (to linear order in θ), to very good approximation, we can determine the frictional behavior by averaging the offset between the trace and retrace directions in the lateral signal over the regions in Fig. 3 in order to determine a W_V for each applied load L. This was achieved by taking three groups of 5 line scans at each load to determine an average W_V along with its standard deviation (taken as the error for this experimentally determined value). The adhesion at each load value was estimated as the average value of the pull off force of the tip from the graphene surface measured both before and after each scan. In the data acquisition, we first performed the low-load measurements (below 10 nN applied load) and found a roughly constant adhesion of 3.7 ± 0.3 nN, while the higher-load measurements were acquired afterwards with the same tip and had an increased adhesion of 4.3 ± 1.0 nN. In order to access the regime close to zero net load (having negative L), we first applied a set-point load to the tip slightly exceeding the magnitude of the measured adhesion by approximately 2 nN so that the tip engaged the surface. The set-point of L was then reduced and fixed at a negative value, while still maintaining a positive net load, followed by the acquisition of an entire scanned image.

Figure 5(a) shows a plot of the measured W_V versus the net load (the applied load added to the measured adhesion, i.e., $L + A$), which shows a sub-linear response. To perform the low-load non-linear calibration requires the value of the derivative $\frac{dW_V}{d(L+A)}$. This derivative is obtained from the W_V data by first performing a weighted fit to the W_V of the power-law form $C(L + A)^p$, with the constants C and p being the fitting parameters varied in order to minimize the χ^2. This fit yielded a value for the power, p, of 0.66 ± 0.01, which is consistent with a stiff single asperity tip-surface contact (as discussed in more detail further below).[36] The fit, shown in Fig. 5(a), was used to calculate $\frac{dW_V}{d(L+A)}$ for each value of $(L+A)$ in the analysis.

Figure 6 shows a comparison between the surface angle calculated from the topography, θ_{topo}, and θ_{lfm} (i.e., either θ_{norm} or θ_{vert}) calculated from the lateral signal obtained using Eqs. (15) and (16) for various net loads (for both linear and non-linear frictional models). The surface angle, $\theta_{topo}(x)$, is

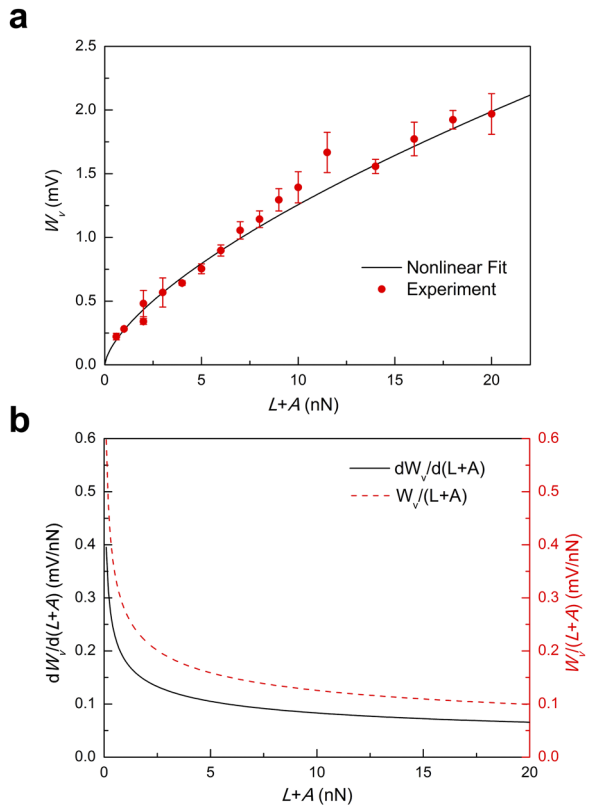

FIG. 5. Nonlinear lateral force signal W_V versus net load. (a) Experimental values of W_V versus net load showing nonlinearity. The nonlinear fit is of the form $c(L + A)^p$ with $p = 0.66 \pm 0.01$. Each data point is an average of 5 adjacent lines. The lateral force signal W_V is proportional to the nonlinear frictional curve. (b) Comparison of the derivative $\frac{dW_V}{d(L+A)}$ with $\frac{W_V}{(L+A)}$, as a function of net load.

determined by taking a numerical derivative at each fast-scan position (x) of the average of 5 line scans (equivalent to approximately 2.9 nm along the slow-scan direction) of topographic data. To determine $\theta_{lfm}(x)$, a low pass filter is first applied to $V_t(x)$ and $V_r(x)$ to remove high frequency noise, and they are then converted to 3rd order interpolated functions.

To account for slight horizontal shifts in the AFM scanner between the trace and retrace data, a constant offset, x_{offset}, between the trace and retrace of the topography data is found by minimizing $\int |H_t(x) - H_r(x + x_{offset})|dx$ with respect to the free parameter x_{offset}. This value is then used to shift $V_r(x)$ relative to $V_t(x)$. For our AFM-sample system, we find the offset to generally range between 0 and 5 nm, with an average value of 3.1 nm. The half difference, $W_V(x) = \frac{V_t(x) - V_r(x+x_{offset})}{2}$, and the zeroed average, $\Delta_{V_0}(x) = \frac{V_t(x)+V_r(x+x_{offset})}{2} - V_0$, are then calculated with V_0 determined by taking the spatially averaged value of $V_t(x)$ and $V_r(x + x_{offset})$ over the entire scan. $\theta_{norm}(x, \alpha)$ and $\theta_{vert}(x, \alpha)$ are subsequently calculated using Eqs. (15) and (16).

The calibration constant, α, acts as a scaling factor for θ_{lfm} and is obtained by minimizing $\int (\theta_{lfm}(x, \alpha) - \theta_{topo}(x))^2 dx$ with respect to α. The solid black line in Fig. 7(a) is the function $\theta_{lfm}(\alpha)$ calculated from Eq. (16) and LFM measurements performed at a net load of 10 nN for a single x. This function for $\theta_{lfm}(\alpha)$ intersects the directly determined topographic value θ_{topo} at two possible solutions for α. To resolve this

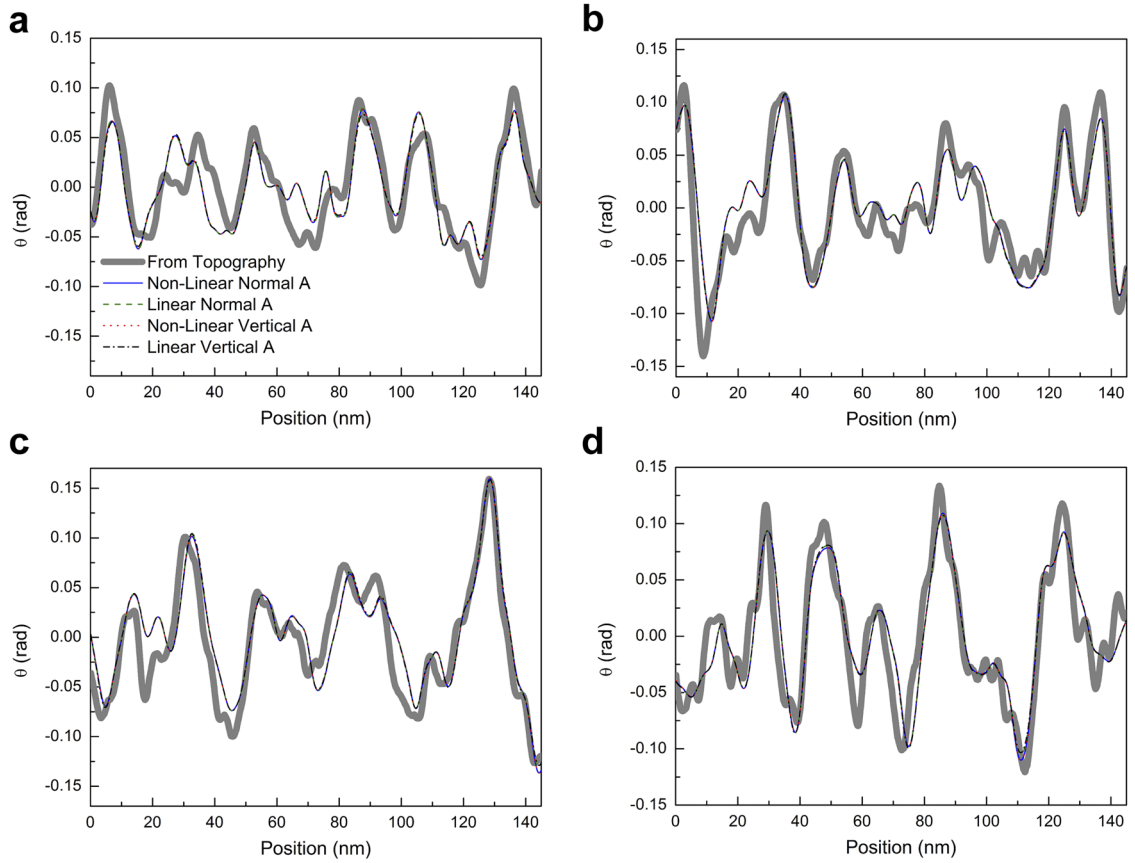

FIG. 6. Comparison of angle as a function of position determined by the topography (θ_{topo}) and lateral signal as calculated with the models discussed in the text (θ_{lfm}). Net loads are 3, 10, 14, and 20 nN for (a), (b), (c), and (d), respectively. A low pass filter has been applied to the data.

ambiguity with low-friction surfaces, $\theta_{lfm}(\alpha)$ can be approximated by a frictionless model, with the term containing α^2 in the denominator of Eq. (16) set equal to zero. There is only one intersection of this frictionless $\theta_{lfm}(\alpha)$ with θ_{topo}, as seen by the dashed blue line in Fig. 7(a), yielding an unambiguous solution in this case. For low-frictional surfaces, like graphene, the friction will contribute a perturbation from this frictionless solution. This makes it easy to determine the correct, physically relevant solution of α according to a frictional model since it is the one that is closest to the unambiguous frictionless value. Figure 7(b) is an expanded view of the plots in Fig. 7(a) that shows the effects of including friction into the determination of the calibration coefficient. A crosscheck to this methodology is obtained by determining the coefficient of friction of the graphene using the resulting calibration coefficient. The smaller α value (i.e., the one closer to that determined from a frictionless model) results in a coefficient of friction of ~0.3 for a 10 nN load, while the larger α value results in a value of ~5, much larger than expected for a single asperity tip on graphene.[38] A resolution in the ambiguity in the determination of α is likewise achieved for the other frictional models assuming both linear and non-linear friction, as well as for the case of normal adhesion described by Eq. (15).

IV. RESULTS AND DISCUSSION

Figure 8 shows the calibration coefficient determined as a function of the net load used for the four different models considered here. The weighted mean calibration coefficients for the four models over the range of $L + A$ = 2–20 nN are α_{L-VA} = 2.69 ± 0.05, α_{NL-VA} = 2.30 ± 0.04, α_{L-NA} = 1.14 ± 0.03, and α_{NL-NA} = 1.15 ± 0.02 nN/mV for the linear vertical adhesion, non-linear vertical adhesion, linear normal adhesion, and non-linear normal adhesion models, respectively. To determine the viability of the possible methods in the low-load regime, we calculate a weighted reduced chi-square (i.e., the "goodness of fit"), χ^2_ν, for the calibration coefficients in the very low net load regime (2–4 nN) with respect to the weighted mean of the calibration coefficient over the extended range (2–20 nN) for the four models. This results in weighted reduced χ^2_ν values of 1.90, 1.11, 235, and 190 for the linear vertical adhesion, non-linear vertical adhesion, linear normal adhesion, and non-linear normal adhesion models, respectively. The models with vertical adhesion clearly result in much more consistent values of α for the low load regime (χ^2_ν = 1.90 and 1.11) compared to the models with normal adhesion (χ^2_ν = 235 and 190), while the non-linear vertical adhesion model is the most self-consistent.

The superiority of the vertical adhesion model for the single asperity tip used in the LFM calibration is also consistent with the expected elastic, geometrical, and adhesive properties of the tip-sample interface. Adhesion at contacts is typically understood within two regimes.[36] One of these regimes (characterized by compliant materials, a large radius of curvature at the contact, and strong short-range adhesive forces) is described well by the Johnson, Kendall, and Roberts (JKR)

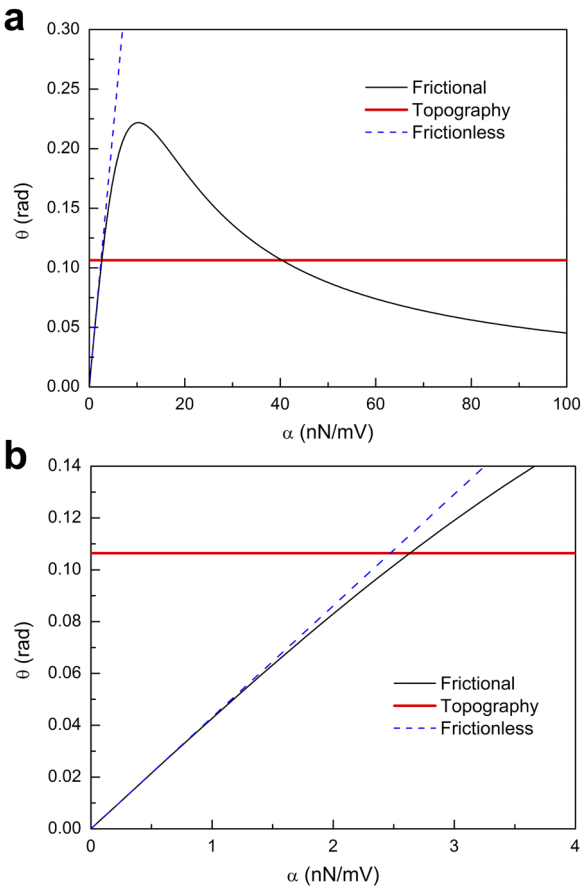

FIG. 7. Determination of the calibration coefficient α obtained by matching the surface angle from topography and the friction model at a single x position. (a) The black-solid line is the calculated surface angle as a function of α, using the frictional non-linear vertical adhesion model of Eq. (16), at a single point with a net load of 10 nN. This angle intersects the value directly determined by the measured topography (the thicker red line) for two possible values of α. A frictionless model (dashed blue line) has only one intersection with the topographically determined value. For low-friction surfaces, like graphene, the physically relevant α value determined by the frictional model is the one closest to the intersection of the frictionless line. (b) Expanded region of (a) showing the intersection of the surface angle measured with the topography and the values calculated with both frictional and frictionless models.

model.[59] The opposite regime (characterized by stiff materials, a small radius of curvature at the contact, and weak long-range adhesive forces) is described well by the Derjaguin, Muller, and Toporov (DMT) model.[60] The crossover between these opposite regimes of a contact is described by Tabor's dimensionless parameter,[61,62] μ_T, with values $\gtrsim 5$ corresponding to the JKR range of validity and for those $\lesssim 0.1$ corresponding to the DMT behavior. Tabor's parameter can be calculated using $\mu_T = \left(\frac{16R\gamma^2}{9K^2 z_0^3}\right)^{1/3}$, where R is the tip radius, $\gamma = \frac{-P_c}{\chi\pi R}$ is the work of adhesion, P_c is the pull off force (which we have identified as the adhesive force in our analysis up to this point), χ is a unitless constant equal to 1.5 in the JKR limit and 2 in the DMT limit, $K = \frac{4}{3}\left(\frac{1-\nu_{tip}^2}{E_{tip}} + \frac{1-\nu_{surface}^2}{E_{surface}}\right)^{-1}$, ν_{tip} and $\nu_{surface}$ are the Poisson ratios for the tip and the surface, E_{tip} and $E_{surface}$ are the elastic moduli for the tip and the surface, and z_0 is the equilibrium separation between the tip and the surface. We estimate Tabor's parameter for our system using a tip radius $R = 10$ nm, a measured pull off force of $P_c = 3$ nN, a lower limit value of $\chi = 1.5$, and an equilibrium separation $z_0 = 0.154$ nm. For the case of a silicon probe on a SiO_2 surface, we use values of E_{tip} in the range of 62–202 GPa, $\nu_{tip} = 0.27$, $E_{surface} = 69$ GPa, and $\nu_{surface} = 0.17$. This results in a range of Tabor's parameter between ~0.16 and 0.21, which is close to the DMT regime and is consistent with the power-law fit, with an exponent of $p \approx 0.66$, to the nonlinear frictional data in Fig. 5(a).[36] That both the nonlinear fit [i.e., Fig. 5(a)] and an estimate of Tabor's parameter indicate that the tip-surface contact should be well-described by the DMT theory is also consistent with a vertical adhesion. In the DMT theory, the adhesion is largely due to attractive forces arising from regions away from the contact.[61] As a result, these attractive forces do not necessarily need to track the small-scale topographic variations that the contact region of the tip makes as it is scanned over the surface with atomic-scale surface roughness.

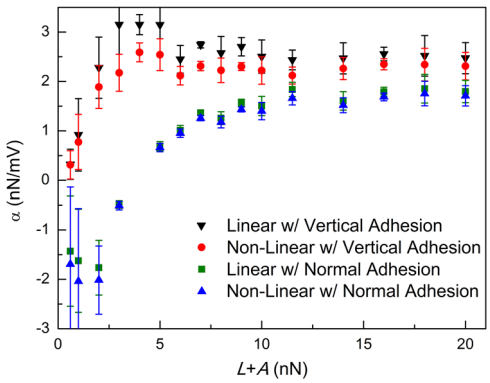

FIG. 8. Lateral calibration constant, α, as a function of net load for the four models. The models with normal adhesion give divergent values of α near $L + A \approx 4$ nN, when $L \approx 0$ nN, that are not plotted and are not included in the averages and goodness of fit determination discussed in the text.

The merging of the calibration coefficients determined by the two adhesion models seen in Fig. 8, as the net load is increased, can be understood from the behavior of Eqs. (15) and (16) used for determining θ in the calibration. As L becomes significantly larger than A, Eqs. (15) and (16) tend to the same form. Although likely dependent on the details of the tip-sample interface, the crossover from non-linear to linear frictional response as the load is increased could likewise cause the results of the models to merge as $L + A$ is increased. Regardless of the details of this crossover in the frictional response, we expect that a sub-linear behavior will yield calibration results that approach the linear model as the load is increased. This can be understood from the nonlinear determination of θ_{vert}, which becomes $\frac{\alpha\Delta_{V_0}}{(L+A)\left[1+p\alpha^2\left(\frac{\alpha C}{(L+A)^{1-p}}\right)^2\right]}$ for a sub-linear response of the form $W_V = C(L+A)^p$. The same sub-linear behavior used in a linear model of θ_{vert} results in $\frac{\alpha\Delta_{V_0}}{(L+A)\left[1+\alpha^2\left(\frac{\alpha C}{(L+A)^{1-p}}\right)^2\right]}$, which differs only by the absence of a factor of p in the second term within the square brackets in the denominator. For sub-linear behavior, with $p < 1$, this second term goes to zero as $L+A$ increases, thus yielding the same θ_{vert} and calibration for both the linear and non-linear expressions. Based on the fits of W_V versus $L + A$ for our probe-sample system, we should expect the percent difference between the non-linear and linear models to drop below 5% for net loads

greater than roughly 5-6 nN. According to the analyzed data in Fig. 8, this crossover occurs at a slightly higher $L+A$, roughly in the range of 11-14 nN, which may be due to additional unaccounted measurement error in the system.

The atomically thin low-profile calibration surfaces we demonstrate here could potentially be useful when deposited directly onto the surfaces of materials that one is interested in investigating through LFM. The conforming nature of the atomically thin 2D materials, such as graphene, would have little impact on the overall elastic response of the AFM-tip-sample system, apart from providing a low-profile low-friction region in which to perform the calibration. This is due to the atomically thin film yielding little impact on the elastic response in the vicinity of the tip-sample interface and to the tip always having nearly the same geometrical orientation with respect to the sample surface (in stark contrast to the case of the standard wedge calibration method[13,18]). Since the elastic behavior in this calibration region (the portion containing the 2D material) should be nearly unchanged from that of the regions of interest (without the 2D material), the resulting calibration should be valid on the surface of the material of interest. This is a potentially important benefit of atomically thin low-profile calibration surfaces because the effective spring constant of the tip-surface interface can have a significant impact on the overall lateral spring constant of the system,[9] which could thus affect the LFM calibration.[23]

In conclusion, we have derived a low-profile LFM calibration method that is applicable in the low-load non-linear regime. The method is particularly attractive for preserving the single asperity LFM tip by performing it on low-friction surfaces, such as exfoliated 2D materials like graphene. Our calibration tests utilizing graphene demonstrate consistency down to applied loads comparable to the tip-sample adhesive forces. Moreover, the modeling of the adhesive forces appears to have the greatest impact on the LFM calibration. Our results indicate that low-profile atomically rough surfaces are best described by a vertical adhesion model, rather than the more commonly utilized one directed normal to the surfaces.

ACKNOWLEDGMENTS

The work was supported by the Department of Energy (DOE) Condensed Matter Physics (CMP) and EPSCoR programs through Grant No. 0000223282, with additional coordinated funds from the Kentucky EPSCoR Program through the Kentucky Science and Technology Corporation (KSTC).

[1]C. M. Mate, G. M. McClelland, R. Erlandsson, and S. Chiang, "Atomic-scale friction of a tungsten tip on a graphite surface," Phys. Rev. Lett. **59**, 1942–1945 (1987).
[2]B. Bhushan, J. N. Israelachvili, and U. Landman, "Nanotribology: Friction, wear and lubrication at the atomic scale," Nature **374**, 607–616 (1995).
[3]G. Binnig, C. F. Quate, and C. Gerber, "Atomic force microscope," Phys. Rev. Lett. **56**, 930–933 (1986).
[4]G. Meyer and N. M. Amer, "Novel optical approach to atomic force microscopy," Appl. Phys. Lett. **53**, 1045–1047 (1988).
[5]A. L. Weisenhorn, P. K. Hansma, T. R. Albrecht, and C. F. Quate, "Forces in atomic force microscopy in air and water," Appl. Phys. Lett. **54**, 2651–2653 (1989).
[6]J. L. Hutter and J. Bechhoefer, "Calibration of atomic-force microscope TIPS," Rev. Sci. Instrum. **64**, 1868–1873 (1993).
[7]H. J. Butt and M. Jaschke, "Calculation of thermal noise in atomic-force microscopy," Nanotechnology **6**, 1–7 (1995).
[8]N. A. Burnham, X. Chen, C. S. Hodges, G. A. Matei, E. J. Thoreson, C. J. Roberts, M. C. Davies, and S. J. B. Tendler, "Comparison of calibration methods for atomic-force microscopy cantilevers," Nanotechnology **14**, 1–6 (2003).
[9]R. W. Carpick, D. F. Ogletree, and M. Salmeron, "Lateral stiffness: A new nanomechanical measurement for the determination of shear strengths with friction force microscopy," Appl. Phys. Lett. **70**, 1548–1550 (1997).
[10]V. L. Popov, *Contact Mechanics and Friction, Physical Principles and Applications* (Springer-Verlag, Berlin Heidelberg, 2010).
[11]T. Pettersson, N. Nordgren, and M. W. Rutland, "Comparison of different methods to calibrate torsional spring constant and photodetector for atomic force microscopy friction measurements in air and liquid," Rev. Sci. Instrum. **78**, 093702 (2007).
[12]M. Munz, "Force calibration in lateral force microscopy: A review of the experimental methods," J. Phys. D: Appl. Phys. **43**, 063001 (2010).
[13]D. F. Ogletree, R. W. Carpick, and M. Salmeron, "Calibration of frictional forces in atomic force microscopy," Rev. Sci. Instrum. **67**, 3298–3306 (1996).
[14]J. E. Sader, J. W. M. Chon, and P. Mulvaney, "Calibration of rectangular atomic force microscope cantilevers," Rev. Sci. Instrum. **70**, 3967–3969 (1999).
[15]A. Feiler, P. Attard, and I. Larson, "Calibration of the torsional spring constant and the lateral photodiode response of frictional force microscopes," Rev. Sci. Instrum. **71**, 2746–2750 (2000).
[16]R. G. Cain, S. Biggs, and N. W. Page, "Force calibration in lateral force microscopy," J. Colloid Interface Sci. **227**, 55–65 (2000).
[17]G. Bogdanovic, A. Meurk, and M. W. Rutland, "Tip friction–torsional spring constant determination," Colloids Surf., B **19**, 397–405 (2000).
[18]M. Varenberg, I. Etsion, and G. Halperin, "An improved wedge calibration method for lateral force in atomic force microscopy," Rev. Sci. Instrum. **74**, 3362–3367 (2003).
[19]R. J. Cannara, M. Eglin, and R. W. Carpick, "Lateral force calibration in atomic force microscopy: A new lateral force calibration method and general guidelines for optimization," Rev. Sci. Instrum. **77**, 053701 (2006).
[20]Q. Li, K.-S. Kim, and A. Rydberg, "Lateral force calibration of an atomic force microscope with a diamagnetic levitation spring system," Rev. Sci. Instrum. **77**, 065105 (2006).
[21]W. H. Liu, K. Bonin, and M. Guthold, "Easy and direct method for calibrating atomic force microscopy lateral force measurements," Rev. Sci. Instrum. **78**, 063707 (2007).
[22]D. Choi, W. Hwang, and E. Yoon, "Improved lateral force calibration based on the angle conversion factor in atomic force microscopy," J. Microsc. **228**, 190–199 (2007).
[23]F. Wang and X. Z. Zhao, "Effect of contact stiffness on wedge calibration of lateral force in atomic force microscopy," Rev. Sci. Instrum. **78**, 043701 (2007).
[24]M. A. S. Quintanilla and D. T. Goddard, "A calibration method for lateral forces for use with colloidal probe force microscopy cantilevers," Rev. Sci. Instrum. **79**, 023701 (2008).
[25]H. Xie, J. Vitard, S. Haliyo, S. Regnier, and M. Boukallel, "Calibration of lateral force measurements in atomic force microscopy with a piezoresistive force sensor," Rev. Sci. Instrum. **79**, 033708 (2008).
[26]K. H. Chung and M. G. Reitsma, "Note: Lateral force microscope calibration using multiple location pivot loading of rectangular cantilevers," Rev. Sci. Instrum. **81**, 026104 (2010).
[27]K. Wagner, P. Cheng, and D. Vezenov, "Noncontact method for calibration of lateral forces in scanning force microscopy," Langmuir **27**, 4635–4644 (2011).
[28]S. S. Barkley, Z. Deng, R. S. Gates, M. G. Reitsma, and R. J. Cannara, "Quantitative comparison of two independent lateral force calibration techniques for the atomic force microscope," Rev. Sci. Instrum. **83**, 023707 (2012).
[29]R. Alvarez-Asencio, E. Thormann, and M. W. Rutland, "Note: Determination of torsional spring constant of atomic force microscopy cantilevers: Combining normal spring constant and classical beam theory," Rev. Sci. Instrum. **84**, 096102 (2013).
[30]H. B. Wang and M. L. Gee, "AFM lateral force calibration for an integrated probe using a calibration grating," Ultramicroscopy **136**, 193–200 (2014).

[31]N. Mullin and J. K. Hobbs, "A non-contact, thermal noise based method for the calibration of lateral deflection sensitivity in atomic force microscopy," Rev. Sci. Instrum. **85**, 113703 (2014).
[32]D. M. Jarzabek, "Precise and direct method for the measurement of the torsion spring constant of the atomic force microscopy cantilevers," Rev. Sci. Instrum. **86**, 013701 (2015).
[33]B. C. T. Khac and K. H. Chung, "Quantitative assessment of contact and non-contact lateral force calibration methods for atomic force microscopy," Ultramicroscopy **161**, 41–50 (2016).
[34]R. D. Ortuso and K. Sugihara, "The detailed study on the failure of the wedge calibration method at nanonewton setpoints for friction force microscopy," J. Phys. Chem. C **122**, 11464 (2018).
[35]J. P. Gao, W. D. Luedtke, D. Gourdon, M. Ruths, J. N. Israelachvili, and U. Landman, "Frictional forces and Amontons' law: From the molecular to the macroscopic scale," J. Phys. Chem. B **108**, 3410–3425 (2004).
[36]D. S. Grierson, E. E. Flater, and R. W. Carpick, "Accounting for the JKR-DMT transition in adhesion and friction measurements with atomic force microscopy," J. Adhes. Sci. Technol. **19**, 291–311 (2005).
[37]T. Filleter, J. L. McChesney, A. Bostwick, E. Rotenberg, K. V. Emtsev, T. Seyller, K. Horn, and R. Bennewitz, "Friction and dissipation in epitaxial graphene films," Phys. Rev. Lett. **102**, 086102 (2009).
[38]H. Lee, N. Lee, Y. Seo, J. Eom, and S. Lee, "Comparison of frictional forces on graphene and graphite," Nanotechnology **20**, 325701 (2009).
[39]J. S. Choi, J. S. Kim, I. S. Byun, D. H. Lee, M. J. Lee, B. H. Park, C. Lee, D. Yoon, H. Cheong, K. H. Lee, Y. W. Son, J. Y. Park, and M. Salmeron, "Friction anisotropy-driven domain imaging on exfoliated monolayer graphene," Science **333**, 607–610 (2011).
[40]L. Xu, T. B. Ma, Y. Z. Hu, and H. Wang, "Vanishing stick-slip friction in few-layer graphenes: The thickness effect," Nanotechnology **22**, 285708 (2011).
[41]L. Y. Lin, D. E. Kim, W. K. Kim, and S. C. Jun, "Friction and wear characteristics of multi-layer graphene films investigated by atomic force microscopy," Surf. Coat. Technol. **205**, 4864–4869 (2011).
[42]D. P. Hunley, T. J. Flynn, T. Dodson, A. Sundararajan, M. Boland, and D. R. Strachan, "Friction, adhesion, and elasticity of graphene edges," Phys. Rev. B **87**, 035417 (2013).
[43]D. Berman, A. Erdemir, and A. V. Sumant, "Few layer graphene to reduce wear and friction on sliding steel surfaces," Carbon **54**, 454–459 (2013).
[44]M. V. Rastei, B. Heinrich, and J. L. Gallani, "Puckering stick-slip friction induced by a sliding nanoscale contact," Phys. Rev. Lett. **111**, 084301 (2013).
[45]X. Z. Liu, Q. Y. Li, P. Egberts, and R. W. Carpick, "Nanoscale adhesive properties of graphene: The effect of sliding history," Adv. Mater. Interfaces **1**, 1300053 (2014).
[46]M. V. Rastei, P. Guzman, and J. L. Gallani, "Sliding speed-induced nanoscale friction mosaicity at the graphite surface," Phys. Rev. B **90**, 041409(R) (2014).
[47]M. J. Boland, M. Nassari, D. P. Hunley, A. Ansary, and D. R. Strachan, "Striped nanoscale friction and edge rigidity of MoS_2 layers," RSC Adv. **5**, 92165–92173 (2015).
[48]Z. J. Ye and A. Martini, "Atomic friction at exposed and buried graphite step edges: Experiments and simulations," Appl. Phys. Lett. **106**, 231603 (2015).
[49]P. Gallagher, M. Lee, F. Amet, P. Maksymovych, J. Wang, S. P. Wang, X. B. Lu, G. Y. Zhang, K. Watanabe, T. Taniguchi, and D. Goldhaber-Gordon, "Switchable friction enabled by nanoscale self-assembly on graphene," Nat. Commun. **7**, 10745 (2016).
[50]B. Vasic, A. Matkovic, R. Gajic, and I. Stankovic, "Wear properties of graphene edges probed by atomic force microscopy based lateral manipulation," Carbon **107**, 723–732 (2016).
[51]H. J. Lang, Y. T. Peng, and X. Z. Zeng, "Effect of interlayer bonding strength and bending stiffness on 2-dimensional materials' frictional properties at atomic-scale steps," Appl. Surf. Sci. **411**, 261–270 (2017).
[52]P. Gallagher, Y. L. Li, K. Watanabe, T. Taniguchi, T. F. Heinz, and D. Goldhaber-Gordon, "Optical imaging and spectroscopic characterization of self-assembled environmental adsorbates on graphene," Nano Lett. **18**, 2603–2608 (2018).
[53]M. Ishigami, J. H. Chen, W. G. Cullen, M. S. Fuhrer, and E. D. Williams, "Atomic structure of graphene on SiO_2," Nano Lett. **7**, 1643–1648 (2007).
[54]W. Gao and R. Huang, "Effect of surface roughness on adhesion of graphene membranes," J. Phys. D: Appl. Phys. **44**, 452001 (2011).
[55]R. F. Frindt, "Single crystals of MoS_2 several molecular layers thick," J. Appl. Phys. **37**, 1928–1929 (1966).
[56]F. Consador and R. F. Frindt, "Crystal size effects on the exciton absorption spectrum of WSe_2," Phys. Rev. B **2**, 4893–4896 (1970).
[57]K. S. Novoselov, A. K. Geim, S. V. Morozov, D. Jiang, Y. Zhang, S. V. Dubonos, I. V. Grigorieva, and A. A. Firsov, "Electric field effect in atomically thin carbon films," Science **306**, 666–669 (2004).
[58]O. Zworner, H. Holscher, U. D. Schwarz, and R. Wiesendanger, "The velocity dependence of frictional forces in point-contact friction," Appl. Phys. A: Mater. Sci. Process. **66**, S263–S267 (1998).
[59]K. L. Johnson, K. Kendall, and A. D. Roberts, "Surface Energy and contact of elastic solids," Proc. R. Soc. A **324**, 301–313 (1971).
[60]B. V. Derjaguin, V. M. Muller, and Y. P. Toporov, "Effect of contact deformations on adhesion of particles," J. Colloid Interface Sci. **53**, 314–326 (1975).
[61]D. Tabor, "Surface forces and surface interactions," J. Colloid Interface Sci. **58**, 2–13 (1977).
[62]J. A. Greenwood, "Adhesion of elastic spheres," Proc. R. Soc. A **453**, 1277–1297 (1997).